



HAL
open science

Finite volume release non-Boussinesq gravity flows on slopes

Jocelyn Étienne, Emil J Hopfinger

► **To cite this version:**

Jocelyn Étienne, Emil J Hopfinger. Finite volume release non-Boussinesq gravity flows on slopes. 7th Internatioanl Symposium on Stratified Flows, Aug 2011, Rome, Italy. hal-04081573

HAL Id: hal-04081573

<https://hal.science/hal-04081573>

Submitted on 25 Apr 2023

HAL is a multi-disciplinary open access archive for the deposit and dissemination of scientific research documents, whether they are published or not. The documents may come from teaching and research institutions in France or abroad, or from public or private research centers.

L'archive ouverte pluridisciplinaire **HAL**, est destinée au dépôt et à la diffusion de documents scientifiques de niveau recherche, publiés ou non, émanant des établissements d'enseignement et de recherche français ou étrangers, des laboratoires publics ou privés.



Distributed under a Creative Commons Attribution 4.0 International License

Finite volume release non-Boussinesq gravity flows on slopes

Jocelyn Étienne and Emil J. Hopfinger

CNRS – Université Joseph Fourier, Grenoble
Laboratoire Interdisciplinaire de Physique (LiPhy)
BP 53, F-38402 Saint-Martin-d'Hères
Jocelyn.Etienne@ujf-grenoble.fr

CNRS
Laboratoire des Écoulements Géophysiques et Industriels (LEGI)
BP 53, F-38041 Grenoble
Emil.Hopfinger@hmg.inpg.fr

Abstract

Finite volume release gravity currents of large density contrasts on steep slopes are simulated numerically using a dynamic mesh adaptation technique. This technique allows to treat large Reynolds numbers and large density differences but it is (presently) restricted to two dimensions. Comparison of numerical results with experiments in the Boussinesq limit shows that these simulations capture the essential dynamics. Large density contrast simulations are then presented, allowing to analyse the behaviour of dense clouds on steep slopes. It is shown that large density clouds accelerate over much larger distances and that their spatial growth in height decreases substantially. The maximum velocity inside the cloud, relative to the front velocity, decreases from about a factor of 2 in the Boussinesq limit to about 1.3 when the density ratio is 20. Non-Boussinesq clouds are found to consist of a relatively dense layer near the bottom and a dilute layer above.

1. Introduction

Gravity driven flows on slopes are frequently encountered in nature. Examples are dust storms, katabatic winds, turbidity current in the ocean, pyroclastic flows and powder-snow avalanches (see Turner, 1973; Simpson, 1997). In the latter examples the density difference is due to the extra weight of suspended solid particles and density variations can be large. Often, these currents are not permanent and consist of a head followed by a quasi steady current. The importance of the layer behind the head depends on the inflow conditions of which two limiting cases are either a continuous source or a finite volume release of heavy fluid. Laboratory experiments of gravity currents on inclined boundaries with emphasis on the head were conducted by Britter and Linden (1980). Beghin et al. (1981) and Maxworthy and Nokes (2007) investigated finite volume release clouds on slopes. These laboratory experiments were done for Boussinesq conditions and there are virtually no experimental results available for non-Boussinesq currents or clouds. Only non-Boussinesq lock-exchange flows were studied experimentally by Gröbelbauer et al. (1993) and recently by Lowe et al. (2005). Étienne et al. (2005) performed numerical simulations, using a dynamic mesh adaptation technique, of very large density ratio exchange flows including the experimental conditions (density ratio of 20) of Gröbelbauer et al. Non-Boussinesq numerical simulations of lock-exchange flows of lower density ratios (< 5), corresponding to the experiments of Lowe et al., were conducted by Birman et al. (2005). The simulations by Étienne et al. showed a Reynolds number dependency of the front velocity when Re was below a certain value. The non-uniform mesh, with dynamic grid adaptation, used in these simulations allowed reaching large enough Reynolds numbers. No direct numerical simulations of unsteady

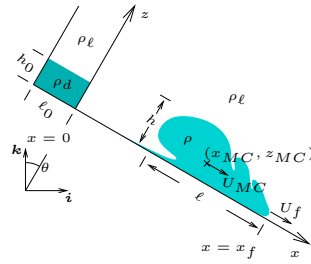


Figure 1: Front velocity, height and length of the cloud. Area $h_0\ell_0$ is 1, ℓ_0/h_0 is 3.

gravity flows on inclined boundaries seem to exist, other than the ones in Boussinesq conditions by Étienne et al. (2004, 2006). Of particular interest, for avalanches and pyroclastic flows especially, are the head of gravity current and the finite volume release cloud structure. Rastello and Hopfinger (2004) proposed a model allowing extrapolating laboratory experiments obtained for Boussinesq clouds to non-Boussinesq conditions. This model indicates that the spatial growth in height of the cloud is substantially reduced when the density difference is large and that inside the cloud, near the bottom, the velocity with respect to the front velocity decreases. It was assumed that the growth in length is independent of density difference. Observations of powder-snow avalanches (see Rastello and Hopfinger) qualitatively support this model and conjectures. In order to make progress in the understanding of the cloud structure and evolution, Direct Numerical Simulations (DNS) or Large Eddy Simulations (LES) are useful.

In Section 2, the governing equations and flow conditions are presented. Section 3 contains results for Boussinesq clouds and in Section 4 the effects of large density contrasts are outlined.

2. Flow conditions and governing equations

2.1. Flow conditions and behaviour

The flow configuration considered in this paper is sketched in figure 1. A closed, rectangular domain $\Omega = (-\ell_0, L_0) \times (0, H_0)$ is taken in the plane (x, z) , the z -axis is at an angle $\theta = 32^\circ$ with respect to the vertical direction. The domain is initially filled with a fluid of density ρ_ℓ , the ambient fluid, except for the region $(-\ell_0, 0) \times (0, h_0)$, which is filled with a fluid of density $\rho_d > \rho_\ell$, miscible with the ambient fluid. Both fluids are at rest. At time $t = 0$, the boundary between the two fluids is removed and the gravitational acceleration sets the dense fluid into motion, forming a cloud which flows down the sloping boundary $z = 0$. A shear layer develops at the top interface of this cloud and the ambient fluid, and the two fluids are mixed by turbulent mixing and ultimately by diffusion.

Experimental investigation of the flow produced under these conditions and for small density ratio (table 1) were conducted by Beghin et al. (1981); Hermann et al. (1987) and Rastello and Hopfinger (2004). Two essential results arise from these experiments. Firstly, the force balance is between the driving buoyancy force and the entrainment of ambient fluid into the cloud. As ambient fluid is entrained it has to be accelerated, and this momentum transfer results in an effective drag, which has an effect of a much larger magnitude than ground friction. There is practically no flow separation, so that the form drag is negligible; the interfacial friction is included in the entrainment. As a result of entrainment, the cloud grows in height and length, but its aspect ratio remains similar. Secondly, it was shown that entrainment of ambient fluid

Ref.	Fluids employed	Boundary conditions	$\alpha = \frac{\rho_d - \rho_\ell}{\rho_\ell}$	$\text{Re} = \frac{\rho_\ell L \sqrt{\alpha g L}}{\eta}$
E1	Brine and fresh water experiment		0.02	$1.2 \cdot 10^4$
E2	Brine and fresh water experiment		0.05	$2.7 \cdot 10^4$
N3	<i>Numerical simulation</i>	No slip	0.02	10^5
N4	<i>Numerical simulation</i>	No friction	0.02	10^5
N5	<i>Numerical simulation</i>	No friction	0.02	10^4
N6	<i>Numerical simulation</i>	No friction	3	10^5
N7	<i>Numerical simulation</i>	No friction	9	10^5
N8	<i>Numerical simulation</i>	No friction	19	10^5

Table 1: Nomenclature of experiments and numerical simulations. Experiment (E1) is by Beghin et al. (1981) and experiment (E2) by Rastello and Hopfinger (2004).

is caused by the overturning motion of the large structures of the flow. These structures, which are similar to Kelvin–Helmholtz billows and appear at the interface between the cloud and ambient fluid, are generated by an essentially two-dimensional mechanism. Three-dimensional turbulent structures of smaller scale are superimposed on the large structure, and it can be expected that their effect on the flow is of second order. This is the case in lock-exchange flows (see Härtel et al., 2000; Étienne et al., 2005). The experimental clouds were found to accelerate initially with a front velocity $U_f \propto \sqrt{x_f}$, where x_f is the position of the front along the slope, and then to decelerate from some point x_f^* , which depends on the density difference and the slope. Field observations of large density difference gravity currents, notably powder-snow avalanches, show that the aspect ratio of avalanche length to height is clearly much larger. In order to highlight the large density difference effect on the flow structure, the conditions in the numerical simulations are kept the same (same volume of dense fluid and same slope angle); only the initial density was varied as indicated in table 1.

2.2. Governing equations and numerical technique

We consider the isothermal flow of a binary mixture of fluids of different densities, and equal, constant dynamic viscosity. For a perfect mixture of two incompressible fluids, of density ρ_d (the heavier one) and of density ρ_ℓ (the lighter one), the local density is $\rho = \rho_d \Phi + \rho_\ell (1 - \Phi)$, where Φ is the local volume fraction of the fluid of density ρ_d . The density contrast is defined as $\alpha = (\rho_d - \rho_\ell) / \rho_\ell$, so that in terms of α , the density is $\rho = \rho_\ell (1 + \alpha \Phi)$. Lengths are non-dimensionalized by the characteristic length scale $L = \sqrt{h_0 \ell_0}$, $x = \tilde{x} / L$ and velocities by the terminal velocity $U = \sqrt{\alpha g L}$ of a fluid element of density ρ_d in the ambient fluid of density ρ_ℓ , $\mathbf{u} = \tilde{\mathbf{u}} / U$. Times are non-dimensionalized as $t = \tilde{t} U / L$. Momentum and mass conservation of the cloud and ambient fluid are given by the Navier–Stokes equations,

$$(1 + \alpha \Phi) \frac{D\mathbf{u}}{Dt} = -\nabla p + \frac{1}{\text{Re}} \nabla \cdot \left[\lambda(\Phi) \left(2\mathbb{D}\mathbf{u} - \frac{2}{3} \nabla \cdot \mathbf{u} \mathbb{I} \right) \right] - \frac{1 + \alpha \Phi}{\alpha} \mathbf{k} \quad (1)$$

$$\alpha \frac{D\Phi}{Dt} + (1 + \alpha \Phi) \nabla \cdot \mathbf{u} = 0 \quad (2)$$

where the Reynolds number is defined as $\text{Re} = \rho_\ell U h / \eta$, $\lambda = \mu(\Phi) / \eta$ and $\mathbb{D}\mathbf{u} = (\nabla \mathbf{u} + \nabla \mathbf{u}^T) / 2$. Since the fluids are miscible, we cannot assume $D\rho / Dt = 0$, but rather that there are mass diffusion fluxes in the flow governed by Fick’s law (see Étienne et al., 2005). This yields:

$$\frac{D\Phi}{Dt} + \Phi \nabla \cdot \mathbf{u} = \frac{1}{\text{ReSc}} \nabla^2 \Phi \quad (3)$$

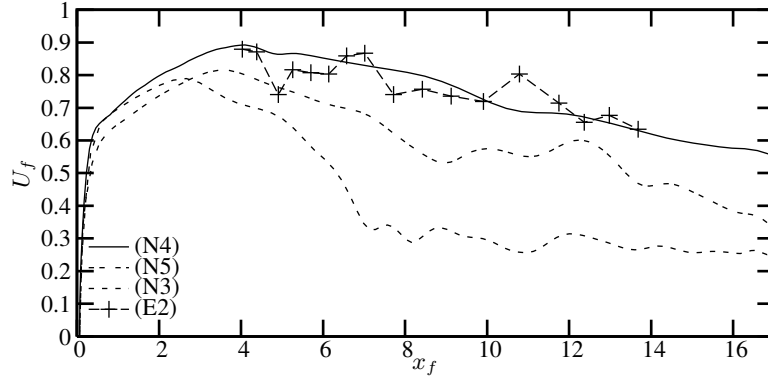


Figure 2: Comparison with experiments of simulated front velocity of the cloud. (N4), $Re = 10^5$ and (N5), $Re = 10^4$, no-friction boundary conditions; (N3), $Re = 10^5$, no-slip boundary conditions; (E2), experimental correlation.

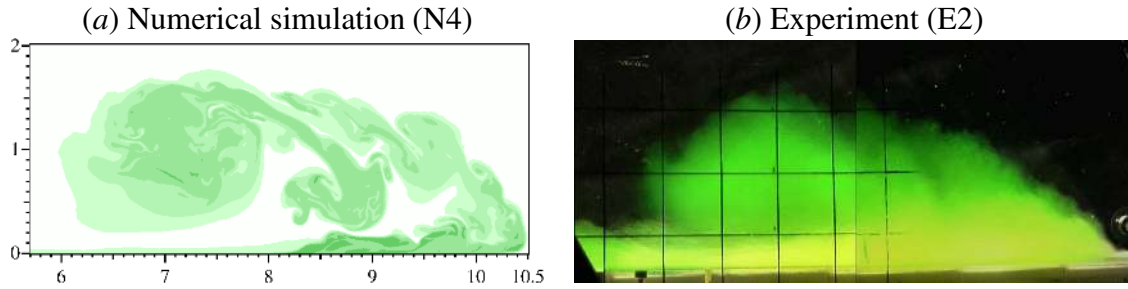


Figure 3: General aspect of (a), the excess density distribution Φ in numerical simulations, and (b), density-marking dye in experiments by Rastello and Hopfinger (2004).

where the Schmidt number is defined as $Sc = \eta/\rho_l \mathcal{D}$, with \mathcal{D} a reference diffusivity. Initial conditions consist of given distribution of ρ , here the dam-break set-up shown in figure 1, the velocity being set to zero everywhere. No inflow or outflow across the boundaries of the flow domain has been considered, thus boundary conditions are always $\nabla \Phi \cdot \mathbf{n} = 0$, with either no-slip boundary conditions ($\mathbf{u}|_{\partial\Omega} = 0$) or zero wall friction ($\mathbf{u} \cdot \mathbf{n} = 0$ and $\sigma \cdot \mathbf{n} - [(\sigma \cdot \mathbf{n}) \cdot \mathbf{n}] \mathbf{n} = \mathbf{0}$, where \mathbf{n} is the wall normal and $\sigma = 2\mathbb{D}\mathbf{u} - \frac{2}{3}\nabla \cdot \mathbf{u} \mathbb{I}$). The Lagrange–Galerkin algorithm proposed by Étienne and Saramito (2005) for system (1–3) is used with a quadratic finite element (see Hood and Taylor, 1973) for the velocity and volume fraction. The mesh adaptation is an iterative process: for each timestep, a first guess of the solution is calculated on a uniform coarse mesh, and is used to generate a new mesh on which a better approximation of the solution can be calculated. We iterate this procedure 4 times, the final mesh has refinement ratios of order 10^3 between the coarsest triangle size and the finest one.

A list of conditions for which numerical simulations were conducted is given in Table 1. The aspect ratio of the released volume is $\ell_0/h_0 = 3$ in all the simulations presented here. Other initial aspect ratios as well as a linearly stratified initial fluid volume have been tested but were found to affect the results over a short time only.

3. Comparison of simulations with laboratory experiments in the Boussinesq limit

Boussinesq conditions correspond to the case of $\alpha \ll 1$, equations (1,2) thus reduce to:

$$\frac{D\mathbf{u}}{Dt} = -\nabla p' + \frac{1}{Re} \nabla \cdot (2\lambda(\Phi)\mathbb{D}\mathbf{u}) - \Phi \mathbf{k}, \quad (4)$$

$$\nabla \cdot \mathbf{u} = 0, \quad (5)$$

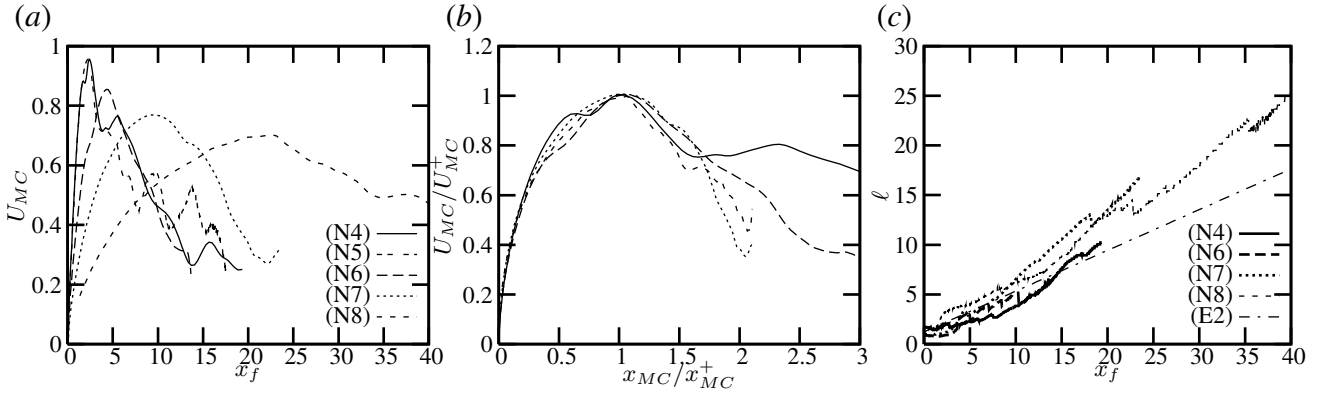


Figure 5: Influence of the Reynolds number and of the density contrast α on the mass center velocity U_{MC} (a,b) and spatial growth of the height (c). Numerical simulations with $\alpha = 0.02$ (N4,N5), $\alpha = 3$ (N6), $\alpha = 9$ (N7) and $\alpha = 19$ (N8). (a), with the velocity non-dimensionalized by $\sqrt{\alpha g L}$ versus front position x_f , and (b), with the velocity normalized by its maximum value U_{MC}^+ versus mass center position x_{MC} normalized by x_{MC}^+ . (c), Heavy lines, numerical results; light lines, model by Rastello and Hopfinger (2004).

4. Numerical results for large density ratios

Clouds of higher density, with $\alpha = 3, 9$ and 19 , respectively, and $Re = 10^5$, are simulated for the same initial conditions and boundary conditions as in the Boussinesq case using constant dynamic viscosity $\lambda(\Phi) = 1$. The change of structure due to large density contrast as compared with Boussinesq conditions is clearly seen in figure 4. The cloud is much more elongated and presents a clear stratification in density with a dense layer near the bottom and a dilute layer above. The head of the current is not as clearly defined. The length of the dashed rectangle in figure 4(b) indicates the length in the x direction over which the density integrated in the z direction is significantly larger than a certain value.

The velocity of the mass center within the indicated rectangle is shown in figure 5. As expected, higher inertia implies a longer running distance before the maximum velocity is reached. There is, however, similarity in the acceleration phase, while the deceleration one is not similar (figure 5(b)). In figure 5(c) the height of the cloud is plotted versus front position for different density contrasts. There is clearly a substantial decrease of the spatial growth in height when the density ratio is large. The straight lines represent, respectively the experimentally determined growth rate (E2) for $\alpha \ll 1$ and the extrapolation to non-Boussinesq clouds proposed by Rastello and Hopfinger (2004), given by $\partial h_{NB}/\partial t = \partial h_B/\partial t (1 + 1/\sqrt{\alpha + 1})/2$. The model predicts qualitatively the decrease of the spatial growth in height when the density ratio is large. However, for $\alpha = 3$ for instance, the simulations indicate practically no effect of density ratio on the spatial growth rate. The length of the cloud head increases considerably with increasing α . This increase is due to the density stratification causing the collapse of the large structures at the rear of the cloud and, hence, a loss of buoyancy to the rear, forming a current rather than a cloud. This is the reason for the more rapid decrease in cloud velocity in the far field.

An important aspect is that the increase of α modifies the distribution of the density in the cloud, with a dense layer near the bottom, visible in the density profiles shown in figure 6. This dense layer is about four times the average density of the cloud. Such a density distribution causes the mass center of the cloud to move closer to the bottom. Figure 6 shows that the velocity near the bottom behind the front is $U_b \simeq 1.3U_f$, which is considerably less than in a Boussinesq cloud. This value corresponds closely to the value of $U_b \simeq 1.23U_f$ predicted by the Bernoulli model proposed by Rastello and Hopfinger (2004).

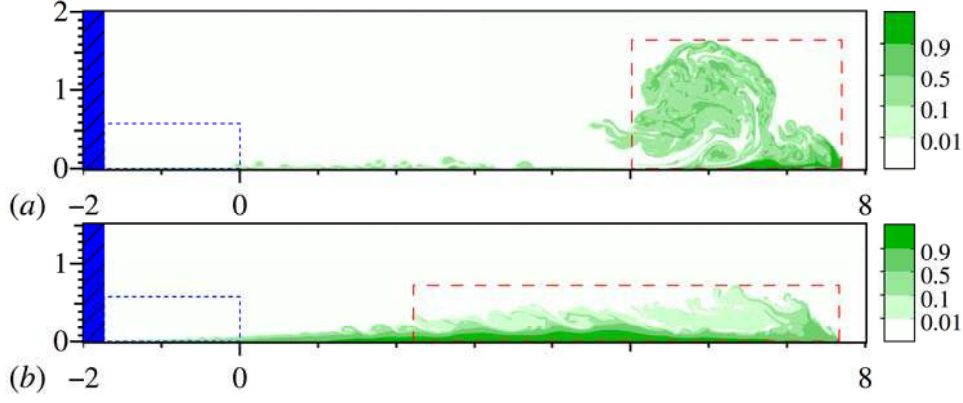


Figure 4: Aspect of simulated clouds for a Boussinesq cloud (a), $\alpha = 0.02$, case (N4); and (b) for $\alpha = 19$, case (N8): gray-level map of Φ in function of x and z . - - -, initial area of the release and —, calculated height and length of the cloud.

where p' is the pressure p minus the hydrostatic pressure. Most of the laboratory experiments are in this limit (e.g., Simpson, 1997; Beghin et al., 1981; Rastello and Hopfinger, 2004), these experiments are used to validate our numerical simulations, and especially the restriction of the simulations to two dimensions. The density ratio is $\alpha = 0.02$, slope is 32° , the reference length $L = 11.4$ cm and velocity $U = 15.0$ cm s $^{-1}$. These conditions are close to those in experiments by Rastello and Hopfinger (2004), where the fluids were brine and fresh water. The reference Reynolds number is 2.7×10^4 ($\alpha = 0.05$). In order to investigate the influence of Reynolds number on the global features of the flow, calculations were performed with $Re = 10^4$ and 10^5 .

Figure 2 shows that two-dimensional simulations with no slip boundary conditions are inappropriate for simulating these flows. This may be due to too large velocity gradients near the boundary in two-dimensional simulations. On the other hand, the front velocity with slip condition simulations is in a good agreement with experiments when $Re = 10^5$. The general aspect of the cloud, shown in figure 3, is similar in numerical simulations and laboratory experiments, dominated by large structures of Kelvin–Helmholtz type. In particular, the height and length of the simulated cloud compare well with experimental laws of Beghin et al. (1981),

$$h_B = [(3.6\theta + 40) \cdot 10^{-3}] (x_f + x_0), \quad \ell_B = [(4.4\theta + 260) \cdot 10^{-3}] (x_f + x_0), \quad (\text{E1})$$

which were obtained in the far-field regime ($x_f \gtrsim 10$), and also the correlation proposed by Rastello and Hopfinger (2004) for the near-field regime ($x_f \in [4; 14]$):

$$h_B = [(3.6\theta + 13) \cdot 10^{-3}] (x_f + x_0). \quad (\text{E2})$$

The common x_0 origin results from a self-similarity assumption; a value $x_0 = 3$ was taken throughout in the figures. The growth of the laboratory cloud is reproduced well by simulations, supporting the hypothesis that the growth is mainly due to the large structures in the shear layer, which are generated by a two-dimensional mechanism. The local large fluctuations in height and length variations are also found in experiments.

When the cloud mass center velocity reaches its maximum, the velocity near the bottom U_b reaches values of $U_b \simeq 2.4U_f$ at a distance of approximately twice the cloud height behind the front. The density near the bottom is still equal to the initial density, $\Phi = 1$. At larger x_f , the density near the bottom decreases but the velocity ratio remains $U_b/U_f \simeq 2$ in agreement with experiments (see Hopfinger and Tochon-Danguy, 1977; Britter and Linden, 1980).

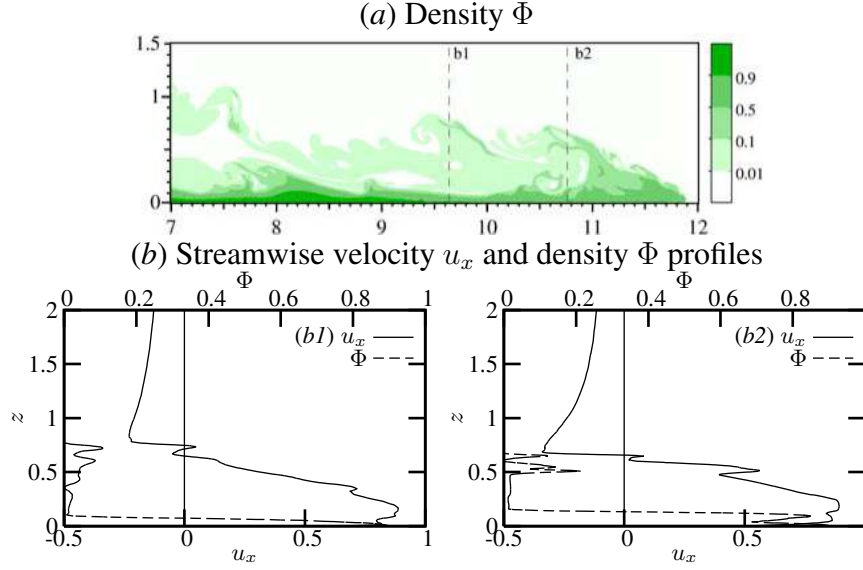


Figure 6: Density and velocity distribution in a high density cloud (N8) as its front reaches $x_f = x_f^*/2$. The front velocity is $U_f \simeq 0.71$, $U_{MC} \simeq 0.59$. Profiles are taken at $x_f - 2h$ (b1) and $x_f - h$ (b2).

It is of interest to examine the Richardson number at collapse of the large eddy structures. This Richardson number is $\text{Ri}_E = \frac{\rho_b - \rho_\ell}{\rho_\ell} g \frac{\tilde{h}_E}{\tilde{U}_E^2} \cos \theta$, where ρ_b is the density near the bottom. Substitution of $\tilde{h}_E = h_E L$ and $\tilde{U}_E = U_E \sqrt{\alpha g L}$, gives:

$$\text{Ri}_E = \frac{\rho_b - \rho_\ell}{\rho_d - \rho_\ell} \frac{\tilde{h}_E}{\tilde{U}_E^2} \cos \theta. \quad (8)$$

In the non-Boussinesq current it is seen from figure 6 that $\rho_b \simeq \rho_d$, $h_E \simeq 0.75$ and $U_E \simeq U_b \simeq 1.3U_f \simeq 1.2$. This gives with $\theta = 32^\circ$ a value $\text{Ri}_E \simeq 0.44$. A stratified shear layer stops growing when the Richardson number is larger than 0.3 when defined with the vorticity layer thickness. It is somewhat larger when defined with the visual thickness. The estimated value of Ri_E is, therefore, consistent with the observed collapse of the cloud and its change-over to a current. In a Boussinesq cloud the eddy velocity $U_E \simeq U_b \simeq 2U_f$. For conditions of figure 4(a), $h_E \simeq 1.5$, $\rho_b - \rho_\ell / \rho_d - \rho_\ell \simeq 0.5$ and $U_E \simeq 2$, giving $\text{Ri}_E \simeq 0.16$.

5. Conclusions

It has been shown that the two-dimensional numerical simulations of non-Boussinesq gravity currents, using dynamic mesh adaptation, capture the essential flow structure and hence the flow dynamics; the force balance is between the gravitational driving force and the drag due to entrainment of ambient fluid. Bottom friction is negligible when the slope angle is large. However, 2D simulations seem to overestimate bottom friction and it has been necessary to impose slip boundary conditions. The numerical simulations have been validated by experiments in the Boussinesq limit. Good agreement with experiments is obtained when the Reynolds number in the simulations is sufficiently large, here of order 10^5 . Large density difference clouds are shown to be much more elongated, due to a reduced spatial growth in height and the collapse of the large structures. The maximum velocity inside the cloud, relative to the front velocity, decreases from a factor of about 2 in the Boussinesq limit to about 1.3 when the density ratio is of order 20. The density variation is substantially modified with a large density layer near the bottom and a fairly dilute layer above.

Acknowledgments

This work was partly supported by the Fonds d'Intervention UJF, Pôle SMINGUE, 2011.

References

- Beghin, P., Hopfinger, E. J., and Britter, R. E. (1981). Gravitational convection from instantaneous sources on inclined boundaries. *J. Fluid Mech.*, 107:407–422.
- Birman, V. K., Martin, J. E., and Meiburg, E. (2005). The non-Boussinesq lock-exchange problem. part 2: high resolution simulations. *J. Fluid Mech.*, 537:125–144.
- Britter, R. E. and Linden, P. F. (1980). The motion of the front of a gravity current travelling down an incline. *J. Fluid Mech.*, 99:531–543.
- Étienne, J., Hopfinger, E. J., and Saramito, P. (2005). Numerical simulations of high density ratio lock-exchange flows. *Phys. Fluids*, 17(3):036601.
- Étienne, J., Rastello, M., and Hopfinger, E. J. (2006). Modelling and simulation of powder-snow avalanches. *C.R. Mécanique*, 334:545–554.
- Étienne, J. and Saramito, P. (2005). A priori error estimates of the Lagrange–Galerkin method for Kazhikhov–Smagulov type systems. *C. R. Mathématiques*, 341:769–774.
- Étienne, J., Saramito, P., and Hopfinger, E. J. (2004). Numerical simulation of dense clouds on steep slopes: application to the powder-snow avalanches. *Annals Glaciol.*, 38:379–383.
- Gröbelbauer, H. P., Fanneløp, T. K., and Britter, R. E. (1993). The propagation of intrusion fronts of high density ratios. *J. Fluid Mech.*, 250:669–687.
- Härtel, C. J. J., Meiburg, E., and Necker, F. (2000). Analysis and direct numerical simulation of the flow at a gravity-current head. Part 1. Flow topology and front speed for slip and no-slip boundaries. *J. Fluid Mech.*, 418:189–212.
- Hermann, F., Hermann, J., and Hutter, K. (1987). Laboratory experiments on the dynamics of powder-snow avalanches. In Salm, B. and Grubler, H., editors, *Avalanches Formation, Movement and Effects (Davos Symposium, Sept. 1986)*, volume 162, pages 431–440. IAHS Publ.
- Hood, P. and Taylor, C. (1973). A numerical solution of the Navier-Stokes equations using the finite element technique. *Comput. & Fluids*, 1(1):73–100.
- Hopfinger, E. J. and Tochon-Danguy, J.-C. (1977). A model study of powder-snow avalanches. *J. Glaciol.*, 19(81):343–356.
- Lowe, R. J., Rottman, J. W., and Linden, P. F. (2005). The non-boussinesq lock-exchange problem. part 1. theory and experiments. *J. Fluid Mech.*, 537:101–124.
- Maxworthy, T. and Nokes, R. I. (2007). Experiments on gravity currents propagating down slopes. part 1. the release of a fixed volume of heavy fluid from an enclosed lock into an open channel. *J. Fluid Mech.*, 584:433–453.
- Rastello, M. and Hopfinger, E. J. (2004). Sediment-entraining suspension clouds: a model of powder-snow avalanches. *J. Fluid Mech.*, 509:181–206.
- Simpson, J. (1997). *Gravity currents in the Environment and the Laboratory*. Cambridge University Press. 2nd ed.
- Turner, J. S. (1973). *Buoyancy effects in fluids*. Cambridge University Press.